Substructure elimination and binding method for vibration systems governed by a one-dimensional wave equation

Keisuke YAMADA* and Jinchen JI**

*Faculty of Engineering Science, Kansai University
3-3-35 Yamate-cho, Suita-shi, Osaka 564-8680, Japan
E-mail: yamadak@kansai-u.ac.jp
**School of Mechanical and Mechatronic Engineering, University of Technology Sydney
Ultimo, NSW 2007, Australia

Abstract

This paper presents a vibration analysis using the substructure elimination and binding method for vibration systems governed by a one-dimensional wave equation. Coupled vibration analysis has been developed, and the component mode synthesis method is commonly used for dynamic analysis. In the component mode synthesis method, each substructure is formulated, and then coupling between substructures is considered. The component mode synthesis method is a type of modal analysis, and the coupled vibration between vibration systems with different governing equations can be easily formulated. The component mode synthesis method has the problem of increasing the degrees of freedom when the entire structure is complicated and needs to be divided into many substructures. Therefore, the first author proposed methods to analyze the entire vibration system without dividing it into substructures, for example, when a structure is installed inside an acoustic field or when acoustic fields with different media are in contact. These methods have the advantage that only the eigenmodes of the entire acoustic field are used. However, the calculation accuracy has been found to deteriorate because of the discontinuities or non-smooth points in sound pressure and particle displacement at the interface between air and a structure or between two acoustic fields. This study proposed a method to set a virtual elimination region at the interface and then bind the two ends of the virtual elimination region to solve this problem. The analytical model for this method was presented, and a wave equation was derived in this study. Modal analysis was applied to the wave equation. The simulations revealed that the density and bulk modulus of the virtual elimination region should be zero and that its length should be set at 2.5–3.5 times the wavelength of the highest eigenmode of the entire vibration system. To investigate the advantage of low DOFs, the simulation results obtained using the proposed method were compared with those obtained using the component mode synthesis method based on the exact solutions.

Keywords : Wave equation, Modal analysis, Coupled vibration, Continuum vibration, Acoustic field, Simulation

1. Introduction

Numerical analysis methods are indispensable for vibration analysis. Coupled vibration analysis methods between multiple structures and between acoustic fields and structures have been developed. The development of coupled vibration analysis cannot be explained without using the substructure synthesis method (Hale and Meirovitch, 1980; Ookuma and Nagamatsu, 1985, 1986; Shabana, 1985). In the substructure synthesis method, the entire structure is divided into several substructures. For dynamic analysis, the component mode synthesis method (CMSM) is used among the various methods classified as substructure synthesis methods. The vibration of each substructure is expressed by the superposition of the eigenmodes of each substructure in the CMSM. In this method, each substructure is formulated, and the coupling between the substructures is considered. The CMSM can easily formulate coupled vibrations between vibration systems with different governing equations, such as coupled vibrations between acoustic fields and structures. CMSM is a type of modal analysis, and the ease of analyzing coupled vibrations is a feature of modal analysis (Benaroya

and Nagurka, 2009; Meirovitch, 1967, 1990, 2001; Nagamatsu, 1985; Rao, 2007; Reismann, 1988; Shabana, 1991; Yamada and Utsuno, 2015, 2020). In the simulations conducted in this study, the results of the proposed method were compared with those of a method that used boundary conditions to obtain exact solutions (Bishop and Johnson, 1960; Tanaka et al., 2012). Because an analysis method that uses boundary conditions to obtain exact solutions does not use modal analysis, many coupled vibrations cannot be formulated using this method. For example, the coupled vibration when an elastic plate is installed on the sidewall of a one-dimensional acoustic tube cannot be formulated using this method. A CMSM is versatile, and various types of coupled vibrations can be formulated using this method. However, the CMSM has the problem of increasing the degrees of freedom (DOFs) when the entire structure is complicated and must be divided into many substructures. Therefore, the first author presented a method for analyzing the vibration of an acoustic field with acoustic absorption materials installed in a part of the acoustic field or a structure installed inside the acoustic field without dividing the entire structure into substructures (Yamada, 2017, 2018, 2020). This method expresses the vibration of the entire structure by the superposition of the eigenmodes of the entire structure without acoustic absorption materials or the installed structure. The superposition of the eigenmodes of the entire structure is essentially a series, and the vibration can be expressed by this series when acoustic absorption materials and structures are installed inside the entire structure. Because this method uses only the superposition of the eigenmodes of the entire structure, in which nothing is installed, the DOFs do not increase even if the entire structure is complicated. However, the calculation accuracy of this method has been found to deteriorate because of the discontinuities or non-smooth points in sound pressure and particle displacement at the interface between air and acoustic absorption material or structure. Although coupled vibrations involving the acoustic field were described as representative here, the essence is the same for the longitudinal vibration of thin rods, the transverse vibration of strings, and the bending vibration of beams, etc. Because the governing equation of a beam differs significantly from those of others, a beam is not described in this study. In this study, vibration systems whose governing equations are expressed by the wave equation are described, and the acoustic field is used as the representative analysis object. In addition, only one-dimensional vibration systems have been described to obtain basic knowledge.

The authors also proposed a substructure elimination method (SEM), which uses only the superposition of eigenmodes of the entire structure (Yamada, 2017, 2018; Yamada and Ji, 2023a, 2023b). When SEM was applied to a one-dimensional acoustic field, elimination regions with zero density and zero bulk modulus were first set at both ends of the acoustic field. Arbitrary boundary conditions were then applied to the new boundaries using the constraint conditions. This method uses the superposition of eigenmodes before setting elimination regions at both ends. If a 1-DOF vibration system is installed at the new boundary, the coupled vibration between the acoustic field and the structure can be analyzed. This coupled vibration can also be analyzed without setting elimination regions by a method, which is classified as CMSM. By comparing the simulation results of these two methods, it was found that SEM provided simulation results with sufficient precision and fewer DOFs. This is because the eigenfunctions exhibited phase variations at the new boundaries in SEM. Conversely, in the CMSM, the eigenfunctions have only two types of phases at the boundaries: in-phase and anti-phase. SEM can tune the amplitude and phase at new boundaries with the superposition of fewer eigenmodes because of phase variation.

Inspired by SEM, this study proposes a method to set a virtual elimination region at the interface and then bind the two ends of the virtual elimination region to solve the problem of deterioration of the simulation precision caused by discontinuities or non-smooth points in the sound pressure and particle displacement at the interfaces. Although this virtual elimination region does not exist, it is set in the analytical model. Within this virtual elimination region, the sound pressure is zero because the density and bulk modulus are set to zero. However, the particle displacement can assume any value. This allows the particle displacement to be connected continuously and smoothly. The two ends of the virtual elimination region are bound using constraint conditions. External forces are applied to the two ends of the virtual elimination region to satisfy the constraint conditions. Owing to these external forces, a discontinuity in the sound pressure at the interface can be appropriately expressed. In this study, this method is referred to as the substructure elimination and binding method (SEBM). First, an analytical model of this method is presented. Second, the wave equation for this method is derived, and modal analysis is applied to the wave equation to obtain the equations of motion using modal displacements. Third, the appropriate properties of the virtual elimination region and the highest order of eigenmode are determined through simulations. In this study, the effectiveness of SEBM is verified by comparing the simulation results obtained using SEBM with the exact solutions using boundary conditions. The simulations in this study are performed for vibration systems in which exact solutions can be obtained using boundary conditions. To investigate

the advantage of low DOFs, the simulation results obtained using the SEBM are compared with the simulation results obtained without using the SEBM and the simulation results obtained using the CMSM.

2. Theoretical analysis

In this study, a one-dimensional acoustic field is used as a representative vibration system governed by a one-dimensional wave equation. A case in which the medium is different in a part of the acoustic field and a case in which a 1-DOF vibration system is installed at one point in the acoustic field are considered. In the case of acoustic tubes, the former corresponds to the case in which an acoustic absorption material is installed in a part of the acoustic field, and the latter corresponds to the case in which a plate or a membrane is installed inside the acoustic field. Because a 1-DOF vibration system is used in this study, it corresponds to an analytical model in which only a single vibration mode of the plate or membrane is considered. In the case of strings, the former corresponds to the case in which the line density of a part is different, and the latter corresponds to the case in which a discrete system, such as a mass point, is installed in the string. The former and latter are expressed in a single analytical model. In the analytical model, a virtual elimination region is set at the interface. In this study, SEM is applied, and elimination regions are set at both ends of the acoustic field (Yamada, 2017, 2018; Yamada and Ji, 2023a, 2023b). Assuming that the proposed method is used in the middle of the acoustic field, even if the boundary conditions at both ends of the acoustic field are displacement excitation or closed ends, applying the SEM provides sufficient precision with fewer DOFs than not applying it. This is because it is advantageous to apply SEM to both ends of the acoustic field to express the changes in the eigenfunctions owing to the coupling with fewer DOFs. Both SEBM and SEM set the elimination regions, and these methods should be used in combination as standards to provide sufficient precision with fewer DOFs. First, we present an analytical model of the proposed method. Second, the wave equation of the analytical model is derived, and the constraint equations are formulated. Third, modal analysis is conducted to derive the equations of motion using modal displacements.

2.1 Analytical model

The original analytical model is shown in Fig. 1(a). Here, the left and right regions are referred to as regions A and B, respectively. The air density, bulk modulus, and length of region A are ρ_A, κ_A, and l_A, respectively, and those of region B are ρ_B, κ_B, and l_B, respectively. The left ends of regions A and B are set to the origins of the x_A - and x_B -coordinates, respectively, and the right-hand direction is the positive direction of these coordinates. The acoustic field is excited by a piston at the left-hand end of region A, and a 1-DOF vibration system is installed at the interface between regions A and B. This original analytical model is not used in the SEBM. However, this model is used in Section 3 to derive the exact solutions using the boundary conditions and to formulate the equations of motion using the CMSM (Yamada and Utsuno, 2015). In Fig. 1(a), the x' -coordinate is also shown. The left end of region A is set to the origin of this coordinate, and the right-hand direction is its positive direction. The x' -coordinate is only used in the figures of the simulation results presented in Section 3. The analytical model used in the SEBM is shown in Fig. 1(b). Here, the regions at both ends shown in Fig. 1(b) are the elimination regions of the SEM, the region at the center is the elimination region of the SEBM, and the regions between the left and right elimination regions and central elimination region are regions A and B, respectively. Three elimination regions are installed virtually. For example, there is no length between regions A and B in the actual acoustic field as shown in Fig. 1(a). The cross-sectional area of the acoustic field is uniform and is S;
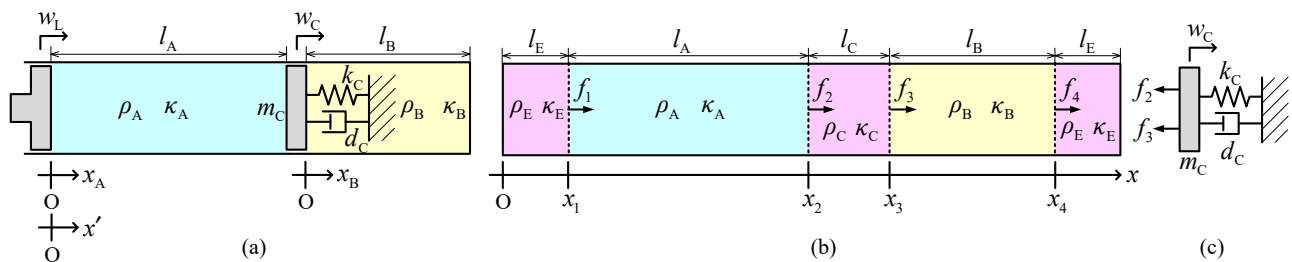

Fig. 1   Analytical models of a one-dimensional acoustic field with a 1-DOF vibration system: (a) original analytical model, (b) analytical model of the acoustic field used in the SEBM with the SEM, and (c) analytical model of a 1-DOF vibration system used in the SEBM with the SEM.

the lengths of the central elimination region and elimination regions at both ends are l_C and l_E, respectively; their air densities are ρ_C and ρ_E, respectively; their bulk moduli are κ_C and κ_E, respectively; the left end of the acoustic field shown in Fig. 1(b) is set to the origin of the x-coordinate; the right-hand direction is the positive direction of the x-coordinate. The x-coordinates of the new left and right boundaries are $x_1(=l_E)$ and $x_4(=l_A+l_B+l_C+l_E)$, respectively, and the x-coordinates of the left and right ends of the central elimination region are $x_2(=l_A+l_E)$ and $x_3(=l_A+l_C+l_E)$, respectively. The overall length of the acoustic field is $l(=l_A+l_B+l_C+2l_E)$. The external forces f_1, f_2, f_3, and f_4 are applied at $x=x_1$, x_2, x_3, and x_4, respectively, in the right-hand direction. These are determined by the constraint conditions. As with SEM, eliminating a region implies that the air density and bulk modulus of the region are set to zero or sufficiently small values such that the sound pressure is zero or almost zero in that region. When the air density and bulk modulus are zero or sufficiently small, the sound pressure is zero or almost zero for all particle displacement values. Therefore, the particle displacement can adopt any value in the central elimination region, and the particle displacement between regions A and B can be smoothly connected.

An analytical model of the 1-DOF vibration system for the SEBM is shown in Fig. 1(c). This 1-DOF vibration system corresponds to a structure installed inside an acoustic field at the interface between regions A and B. The mass, spring constant, viscous damping coefficient, and displacement of the 1-DOF vibration system are m_C, k_C, d_C, and w_C, respectively. The positive direction of the displacement w_C is the right-hand direction. Both f_2 and f_3 are applied to the mass point in the left-hand direction because of the action and reaction relationship, and because the central elimination region does not exist. If the 1-DOF vibration system is not installed in the acoustic field, m_C, k_C, and d_C should be set to zero. The analytical model shown in Figs. 1(b) and (c) can be used to analyze the cases in which the medium of a part of the acoustic field is different and the case in which a 1-DOF vibration system is installed inside the acoustic field as a structure.

As shown in the analytical model, SEM is applied to both ends of the acoustic field. However, because the subject of this study is SEBM, the SEM is not described in detail. In this study, displacement excitation and a closed end are set as the new left and right boundaries at $x=x_1$ and x_4, respectively.

2.2 Wave equation and equations derived by constraint conditions

The wave equation for the analytical model shown in Fig. 1(a) can be derived in a fashion similar to the SEM (Yamada and Ji, 2023). The equation of motion of the minute fraction is expressed as

$$\rho(x)\frac{\partial^2 w}{\partial t^2}=-\frac{\partial p}{\partial x}+\frac{f_1}{S}\delta(x-x_1)+\frac{f_2}{S}\delta(x-x_2)+\frac{f_3}{S}\delta(x-x_3)+\frac{f_4}{S}\delta(x-x_4), \tag{1}$$

$$\rho(x)=\rho_A+\rho_{E\text{-}A}H(x_1-x)+\rho_{C\text{-}A}H(x-x_2)+\rho_{B\text{-}C}H(x-x_3)+\rho_{E\text{-}B}H(x-x_4), \tag{2}$$

$$\rho_{E\text{-}A}=\rho_E-\rho_A,\quad \rho_{C\text{-}A}=\rho_C-\rho_A,\quad \rho_{B\text{-}C}=\rho_B-\rho_C,\quad \rho_{E\text{-}B}=\rho_E-\rho_B, \tag{3}$$

where $\rho(x)$ is the density at the coordinate x; w is the particle displacement; t is the time; p is the sound pressure; δ is the Dirac delta function; and H is the Heaviside step function. Multiplying both sides of Eq. (1) by the cross-sectional area of the acoustic field and the length of the minute fraction dx, the term of the left-hand side is the inertial force of the minute fraction, and the first term on the right-hand side is the force due to the differential pressure on both surfaces of the minute fraction. The second through fifth terms on the right-hand side of Eq. (1) are the external force terms. Because the sound pressure is proportional to the bulk strain, it can be expressed as

$$p(x,t)=-\kappa(x)\frac{\partial w}{\partial x}, \tag{4}$$

$$\kappa(x)=\kappa_A+\kappa_{E\text{-}A}H(x_1-x)+\kappa_{C\text{-}A}H(x-x_2)+\kappa_{B\text{-}C}H(x-x_3)+\kappa_{E\text{-}B}H(x-x_4), \tag{5}$$

$$\kappa_{E\text{-}A}=\kappa_E-\kappa_A,\quad \kappa_{C\text{-}A}=\kappa_C-\kappa_A,\quad \kappa_{B\text{-}C}=\kappa_B-\kappa_C,\quad \kappa_{E\text{-}B}=\kappa_E-\kappa_B, \tag{6}$$

where $\kappa(x)$ is the bulk modulus at the coordinate x. Equations (2) and (5) involve the Heaviside step functions. For example, the value of $H(x_1-x)$ at $x=x_1$ should be determined as follows. When considering the left elimination region and region A, $x=x_1-0$ and $x=x_1+0$ should be used, respectively. The values of $H(x_1-x)$ in the left elimination region and region A are 1 and 0, respectively. Using the displacement potential ψ, the particle displacement

w can be expressed as

$$w(x, t) = -\frac{\partial \psi}{\partial x}.$$ (7)

Substituting Eqs. (4) and (7) into Eq. (1) and integrating both sides with respect to x, the following wave equation using the displacement potential ψ is obtained:

$$\rho(x)\frac{\partial^2 \psi}{\partial t^2} - \rho_{\text{E-A}}H(x_1 - x)\frac{\partial^2 \psi}{\partial t^2}\bigg|_{x=x_1} - \rho_{\text{C-A}}H(x - x_2)\frac{\partial^2 \psi}{\partial t^2}\bigg|_{x=x_2} - \rho_{\text{B-C}}H(x - x_3)\frac{\partial^2 \psi}{\partial t^2}\bigg|_{x=x_3} - \rho_{\text{E-B}}H(x - x_4)\frac{\partial^2 \psi}{\partial t^2}\bigg|_{x=x_4}$$
$$= \kappa(x)\frac{\partial^2 \psi}{\partial x^2} + \frac{f_1}{S}H(x_1 - x) + \frac{f_2}{S}H(x_2 - x) - \frac{f_3}{S}H(x - x_3) - \frac{f_4}{S}H(x - x_4)$$ (8)

The partial differentiation of both sides of the wave equation (8) with respect to x yields the dimensions of the equation of motion given by Eq. (1). For example, the second term on the right-hand side of Eq. (8) can be replaced by $-f_1H(x - x_1)/S$ because $f_1H(x_1 - x)/S$ and $-f_1H(x - x_1)/S$ provide identical expressions when they are partially differentiated with respect to x. Any terms could be used in Eq. (8) if these are equal in the dimensions of Eq. (1). The external force terms in Eq. (8) were determined such that the sound pressures in regions A and B could be formulated using simple expressions.

From Eqs. (4), (7), and (8), the sound pressure can be expressed as

$$p(x, t) = \kappa(x)\frac{\partial^2 \psi}{\partial x^2} = \rho(x)\frac{\partial^2 \psi}{\partial t^2} - \rho_{\text{C-A}}H(x - x_2)\frac{\partial^2 \psi}{\partial t^2}\bigg|_{x=x_2} - \rho_{\text{B-C}}H(x - x_3)\frac{\partial^2 \psi}{\partial t^2}\bigg|_{x=x_3} - \frac{f_2}{S}H(x_2 - x) + \frac{f_3}{S}H(x - x_3).$$ (9)

On the right-hand side of Eq. (9), the terms only for the elimination regions at both ends were omitted. The sound pressure can be obtained from either the middle or right-hand side of Eq. (9). The right-hand side of Eq. (9) is typically more precise because it can express discontinuities using Heaviside step functions. Therefore, the sound pressure was obtained using the right-hand side of Eq. (9) for the simulations conducted in this study.

When the longitudinal vibration of thin rods is analyzed, Young's modulus should be used rather than the bulk modulus in Eq. (8). When the transverse vibration of strings is analyzed, the line density and tension should be used rather than the air density and bulk modulus. The displacement potential can be used in both cases, when the boundary conditions of the original thin rods and strings are assumed to be rigid walls. Equation (7) can be used to derive the displacement of the thin rods and deflection of the strings in each case.

In the wave equation (8), f_1, f_2, f_3, and f_4 are unknown variables. These are determined by the constraint conditions. Because the displacement excitation and closed end are set as $x = x_1$ and x_4, respectively, the following constraint equations can be derived:

$$w(x_1, t) = -\frac{\partial \psi}{\partial x}\bigg|_{x=x_1} = w_{\text{L}}(t), \quad w(x_4, t) = -\frac{\partial \psi}{\partial x}\bigg|_{x=x_4} = 0,$$ (10)

where w_{L} is the displacement imposed by the piston at the new left boundary, although the piston is shown only in Fig. 1(a). Because the particle displacements at $x = x_2$ and x_3 and the displacement of the mass point should be equal, the following constraint equations are obtained:

$$w(x_2, t) = w(x_3, t) = w_{\text{C}}.$$ (11)

Because the displacement w_{C} is also an unknown variable, another equation must be obtained. This is given by the equation of motion for a 1-DOF vibration system, as follows:

$$m_C \ddot{w}_C + d_C \dot{w}_C + k_C w_C = -f_2 - f_3 . \tag{12}$$

Eliminating w_C using Eqs. (11) and (12) leaves only f_1, f_2, f_3, and f_4 as unknown variables. Eliminating w_C means that a 1-DOF vibration system does not have one independent DOF in this method. Equation (12) includes f_2 and f_3, whereas Eqs. (10) and (11) do not. To determine the unknown variables, these particle displacements should be expressed using external forces. Integrating both sides of wave equation (8) from $x = 0$ to x, where $x_1 \le x \le x_2$, we obtain the following equation for the particle displacement in region A:

$$w(x,t) = -\frac{\partial \psi}{\partial x} = -\frac{\rho_A}{\kappa_A} \int_0^x \frac{\partial^2 \psi}{\partial t^2} dx - \frac{\rho_{E\text{-}A}}{\kappa_A} \int_0^{x_1} \frac{\partial^2 \psi}{\partial t^2} dx + \frac{\rho_{E\text{-}A}}{\kappa_A} x_1 \frac{\partial^2 \psi}{\partial t^2}\bigg|_{x=x_1} + \frac{\kappa_{E\text{-}A}}{\kappa_A} \frac{\partial \psi}{\partial x}\bigg|_{x=x_1} + \frac{x_1}{\kappa_A S} f_1 + \frac{x}{\kappa_A S} f_2 , \tag{13}$$

Integrating both sides of wave equation (8) from $x = x$ to l, where $x_3 \le x \le x_4$, we obtain the following equation for the particle displacement in region B:

$$\begin{aligned} w(x,t) = -\frac{\partial \psi}{\partial x} = \frac{\rho_B}{\kappa_B} \int_x^l \frac{\partial^2 \psi}{\partial t^2} dx + \frac{\rho_{E\text{-}B}}{\kappa_B} \int_{x_4}^l \frac{\partial^2 \psi}{\partial t^2} dx - \frac{\rho_{C\text{-}A}}{\kappa_B}(l-x) \frac{\partial^2 \psi}{\partial t^2}\bigg|_{x=x_2} - \frac{\rho_{B\text{-}C}}{\kappa_B}(l-x) \frac{\partial^2 \psi}{\partial t^2}\bigg|_{x=x_3} \\ - \frac{\rho_{E\text{-}B}}{\kappa_B}(l-x_4) \frac{\partial^2 \psi}{\partial t^2}\bigg|_{x=x_4} + \frac{\kappa_{E\text{-}B}}{\kappa_B} \frac{\partial \psi}{\partial x}\bigg|_{x=x_4} + \frac{l-x}{\kappa_B S} f_3 + \frac{l-x_4}{\kappa_B S} f_4 \end{aligned} \tag{14}$$

Using Eqs. (10)–(14), f_1, f_2, f_3, and f_4 can be determined.

The particle displacements in regions A and B can also be calculated using the right-hand sides of Eqs. (13) and (14), rather than the displacement potential gradient. However, if SEM and SEBM were used, the difference would be marginal. This is because the Gibbs phenomenon does not occur in the particle displacement by providing elimination regions. In the simulations in this study, the particle displacement was obtained using the displacement potential gradient.

2.3 Modal analysis

In this section, modal analysis is applied to wave equation (8). The constraint equations are then expressed using the modal displacements.

In the proposed method, the displacement potential ψ is expressed by the superposition of the eigenmodes of the acoustic field, where the elimination regions are not eliminated, and a 1-DOF vibration system is not installed. That is, using the eigenmodes when the density and bulk modulus of the entire acoustic field are ρ_A and κ_A, respectively, and no 1-DOF vibration system is installed, ψ is expressed as

$$\psi(x,t) = \sum_{h=0}^n \Psi_h(x) \xi_h(t), \quad \Psi_h(x) = A_h \cos k_h x, \quad k_h = \frac{h\pi}{l} , \tag{15}$$

where Ψ_h is the eigenfunction of the displacement potential, ξ_h is the modal displacement, subscript h denotes the hth-order eigenmode, n is the highest order of the eigenmode, A_h is an arbitrary constant, and k_h is the wavenumber. Equation (15) represents a Fourier cosine series. From Eqs. (7) and (15), the particle displacement obtained using the displacement potential gradient is a Fourier sine series. In this study, the case in which the density and bulk modulus of the entire acoustic field are ρ_A and κ_A, respectively, is considered. However, the case where they are ρ_B and κ_B can be considered alternatively. Substituting Eq. (15) into wave equation (8), multiplying both sides by Ψ_i / ρ_A, and integrating over the entire range of the acoustic field, the following equations of motion using modal displacements are obtained

$$M_i \ddot{\xi}_i + \frac{\rho_{\text{E-A}}}{\rho_{\text{A}}} \sum_{h=0}^{n} \left(\int_0^{x_1} \Psi_h \Psi_i \, dx - \Psi_h (x_1) \int_0^{x_1} \Psi_i \, dx \right) \ddot{\xi}_h + \frac{\rho_{\text{C-A}}}{\rho_{\text{A}}} \sum_{h=0}^{n} \left(\int_{x_2}^{l} \Psi_h \Psi_i \, dx - \Psi_h (x_2) \int_{x_2}^{l} \Psi_i \, dx \right) \ddot{\xi}_h$$

$$+ \frac{\rho_{\text{B-C}}}{\rho_{\text{A}}} \sum_{h=0}^{n} \left(\int_{x_3}^{l} \Psi_h \Psi_i \, dx - \Psi_h (x_3) \int_{x_3}^{l} \Psi_i \, dx \right) \ddot{\xi}_h + \frac{\rho_{\text{E-B}}}{\rho_{\text{A}}} \sum_{h=0}^{n} \left(\int_{x_4}^{l} \Psi_h \Psi_i \, dx - \Psi_h (x_4) \int_{x_4}^{l} \Psi_i \, dx \right) \ddot{\xi}_h$$

$$+ K_i \xi_i + \frac{\kappa_{\text{E-A}}}{\rho_{\text{A}}} \sum_{h=1}^{n} k_h^2 \int_0^{x_1} \Psi_h \Psi_i \, dx \xi_h + \frac{\kappa_{\text{C-A}}}{\rho_{\text{A}}} \sum_{h=1}^{n} k_h^2 \int_{x_2}^{l} \Psi_h \Psi_i \, dx \xi_h + \frac{\kappa_{\text{B-C}}}{\rho_{\text{A}}} \sum_{h=1}^{n} k_h^2 \int_{x_3}^{l} \Psi_h \Psi_i \, dx \xi_h + \frac{\kappa_{\text{E-B}}}{\rho_{\text{A}}} \sum_{h=1}^{n} k_h^2 \int_{x_4}^{l} \Psi_h \Psi_i \, dx \xi_h$$

$$- \frac{f_1}{\rho_{\text{A}} S} \int_0^{x_1} \Psi_i \, dx - \frac{f_2}{\rho_{\text{A}} S} \int_0^{x_2} \Psi_i \, dx + \frac{f_3}{\rho_{\text{A}} S} \int_{x_3}^{l} \Psi_i \, dx + \frac{f_4}{\rho_{\text{A}} S} \int_{x_4}^{l} \Psi_i \, dx = 0 \quad , \quad (16)$$

$$M_i = \int_0^{l} \Psi_i^2 \, dx = 1, \quad K_i = -c_{\text{A}}^2 \int_0^{l} \Psi_i \frac{d^2 \Psi_i}{dx^2} \, dx = \omega_i^2, \quad c_{\text{A}} = \sqrt{\frac{\kappa_{\text{A}}}{\rho_{\text{A}}}}, \quad \omega_i = \frac{i\pi c_{\text{A}}}{l}, \quad A_i = \begin{cases} \sqrt{1/l} & (i=0) \\ \sqrt{2/l} & (i=1, 2, \cdots) \end{cases}, \quad (17)$$

where M_i and K_i are the modal mass and modal stiffness, respectively, of the original acoustic field without elimination and installing the 1-DOF vibration system; c_{A} is the sound speed in region A; and ω_i is the natural angular frequency of the ith-order eigenmode of the original acoustic field. Wavenumber k_i and natural angular frequency ω_i have the relationship $k_i = \omega_i / c_{\text{A}}$. The arbitrary constant A_i of the eigenfunction was normalized such that $M_i = 1$ in this study. The equation of motion using matrices is expressed as follows:

$$[M]\{\ddot{\xi}\} + [K]\{\xi\} + [Q]\{f\} = \{0\}, \quad \{\xi\} = \{\xi_0 \quad \xi_1 \quad \cdots \quad \xi_n\}^{\text{T}}, \quad \{f\} = \{f_1 \quad f_2 \quad f_3 \quad f_4\}^{\text{T}}, \quad (18)$$

where $[M]$ and $[K]$ are the mass and stiffness matrices, respectively, which are square matrices of size $n+1$; $[Q]$ is the external force influence matrix, which is an $(n+1)$-by-4 matrix; $\{\xi\}$ is the modal displacement vector; $\{f\}$ is the external force vector; and superscript T denotes the transpose of the matrix. Each element of the matrices $[M]$, $[K]$, and $[Q]$ can be obtained using Eq. (16). Although there are several terms on the left-hand side of Eq. (16), the terms related to elimination regions are similar. Therefore, subroutines are useful when the matrices are created using a simulation program.

From Eqs. (10)–(15), the constraint equations can be expressed as

$$\left[C_f \right] \{f\} = [C_a]\{\ddot{\xi}\} + [C_v]\{\dot{\xi}\} + [C_d]\{\xi\} + [C_w]\{w_{\text{L}}\}. \quad (19)$$

Each element of matrices $\left[C_f \right]$, $[C_a]$, $[C_v]$, $[C_d]$ and $[C_w]$ can be determined using Eqs. (10)–(15), and the displacement excitation vector $\{w_{\text{L}}\}$ contains only w_{L} as its element. From Eq. (19), the external force vector $\{f\}$ is derived as follows:

$$\{f\} = \left[C_f \right]^{-1} [C_a]\{\ddot{\xi}\} + \left[C_f \right]^{-1} [C_v]\{\dot{\xi}\} + \left[C_f \right]^{-1} [C_d]\{\xi\} + \left[C_f \right]^{-1} [C_w]\{w_{\text{L}}\}, \quad (20)$$

From Eqs. (18) and (20), the equation of motion using the matrices are expressed as follows:

$$\left([M] + [Q]\left[C_f \right]^{-1} [C_a] \right)\{\ddot{\xi}\} + [Q]\left[C_f \right]^{-1} [C_v]\{\dot{\xi}\} + \left([K] + [Q]\left[C_f \right]^{-1} [C_d] \right)\{\xi\} = -[Q]\left[C_f \right]^{-1} [C_w]\{w_{\text{L}}\}. \quad (21)$$

When $[Q]\left[C_f \right]^{-1} [C_v]$ is a zero vector or is expressed as a linear sum of $[M] + [Q]\left[C_f \right]^{-1} [C_a]$ and $[K] + [Q]\left[C_f \right]^{-1} [C_d]$, that is, when $[Q]\left[C_f \right]^{-1} [C_v]$ is Rayleigh damping, an eigenvalue analysis can be performed using Eq. (21). When $[Q]\left[C_f \right]^{-1} [C_v]$ does not involve Rayleigh damping, eigenvalue analysis should be performed after deriving the equation of state from Eq. (21) for the state-space representation. The uncoupled equations can be derived using the newly obtained eigenvectors from the eigenvalue analysis.

In the simulations conducted in this study, the sound pressures in regions A and B were obtained using the right-hand side of Eq. (9). The right-hand side of Eq. (9) contains the terms for the external forces. The external forces can be obtained using the external force vector $\{f\}$ expressed by Eq. (20). Then, by applying Eq. (20) to Eq. (9), the sound

pressure can be obtained by superposition of the eigenmodes of the original acoustic field. Particle displacement can also be obtained using Eqs. (7) and (15).

3. Verifications through simulation

In this section, the criteria for determining the length, density, and bulk modulus of the central elimination region are established through simulations. A long central elimination region is disadvantageous because the natural frequency of the highest-order eigenmode of the acoustic field is lowered. Preferably, the density and bulk modulus in the central elimination region are zero, because the particle displacement in this region can adopt any value. The case in which the density and bulk modulus of the central elimination region were zero, and only the length of the central elimination region was varied, was considered. Subsequently, the cases in which the density and bulk modulus had small values were considered. In addition, to obtain the criterion for determining the highest order n of the eigenmode of the original acoustic field, the precision of the natural frequencies obtained by the eigenvalue analysis was investigated. As these criteria were also constructed in the study of the SEM (Yamada and Ji, 2023a, 2023b), they were followed in this study. To verify that SEBM with SEM requires fewer DOFs, the simulation results obtained using SEBM with SEM were compared with those obtained using the CMSM (Yamada and Utsuno, 2015). To verify the effectiveness of the central elimination region, the simulation results obtained without setting the central elimination region were also compared. This is referred to as SEM without SEBM. Furthermore, to verify the effectiveness of SEM with SEBM, simulation results obtained using SEBM without SEM were compared. As the exact solutions derived using the boundary conditions were used as the criteria for correctness, the derivation of the exact solutions is briefly described. In addition, the derivation of the equations of motion using the CMSM is briefly described briefly.

3.1 Verification on the length of the central virtual elimination region

The material properties used in the simulations are listed in Table 1. The boundary conditions at $x = x_1$ and x_4 were closed ends. Although the boundary condition at $x = x_1$ was displacement excitation in this study, there is no essential difference between the displacement excitation and the closed end in the eigenvalue analysis. As can be seen from Table 1, both ends of the central elimination region were simply bound. Therefore, the actual acoustic field was essentially a 0.85 m acoustic tube, and the exact natural frequencies were integer multiples of 200 Hz. In these simulations, the relationship between the length of the central elimination region and the precision of the natural frequencies was evaluated. In the simulations, the root mean square (RMS) of the error rates of the natural frequencies obtained using SEBM with SEM was evaluated as the precision of the natural frequencies. Simulations were performed for four cases: $n = 22$, 32, 52, and 92. The 1st–8th-order eigenmodes for $n = 22$, 1st–16th-order eigenmodes for $n = 32$, 1st–32th-order eigenmodes for $n = 52$, 1st–64th-order eigenmodes for $n = 92$ were used to calculate the RMS of the error rates of the natural frequencies. Although the frequency range in which the precise natural frequencies can be obtained is described in Section 3.3, these eigenmodes were used because their natural frequencies can be obtained precisely. $l_E = 0.255$, 0.1275, 0.06375, and 0.031875 [m] were used for $n = 22$, 32, 52, and 92, respectively. The simulation results are presented in Fig. 2(a). The simulation results of the error rate of the first-order natural frequency are shown in Fig. 2(b). The error rate shown in Fig. 2(b) is the magnitude of the error rate when the logarithmic axis is used. The number of wavelengths $A_{\lambda C}$ on the horizontal axis is defined as follows:

$$A_{\lambda C} = \frac{l_C}{\lambda_n}, \quad \lambda_n = \frac{2l}{n}, \tag{22}$$

where λ_n is the wavelength of the highest nth-order eigenmode of the original acoustic field. Similarly, the number of wavelengths of the elimination regions for SEM is defined as

Table 1   Material properties used in the simulations for the verification on the length of the central elimination region.

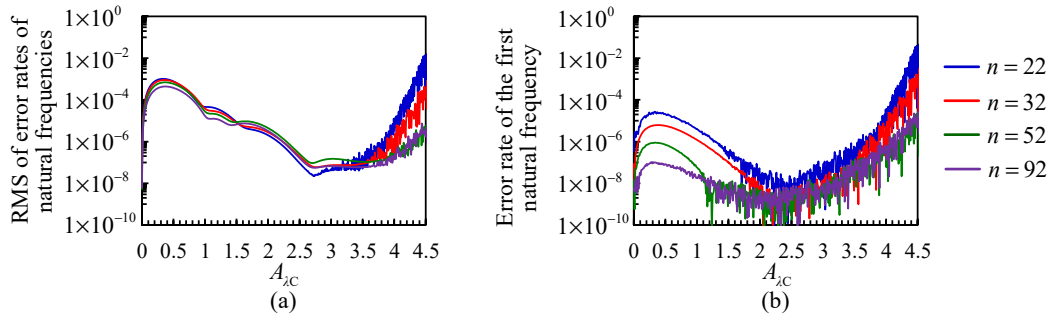| $\rho_A = \rho_B$	1.2 kg/m^3	$\rho_C = \rho_E$	0 kg/m^3	m_C	0 kg
$\kappa_A = \kappa_B$	138720 Pa	$\kappa_C = \kappa_E$	0 Pa	d_C	0 Ns/m
l_A	0.5 m	l_B	0.35 m	k_C	0 N/m

Fig. 2   Simulation results of the error rates of the natural frequencies obtained using the SEBM with the SEM and different values of n: (a) RMS of the error rates of the multiple natural frequencies and (b) magnitude of the error rate of the first-order natural frequency.

$$A_{\lambda E} = \frac{l_E}{\lambda_n}. \tag{23}$$

The natural frequency of the highest nth-order eigenmode of the original acoustic field varies with n, l_C, and l_E. The length l_E was determined such that $A_{\lambda E} = 1.5$ when $A_{\lambda C} = 3$. Therefore, both the natural frequency of the highest nth-order eigenmode and $A_{\lambda E}$ varied with $A_{\lambda C}$ in these simulations. $1.5 \le A_{\lambda E} \le 2$ was recommended in the study of the SEM (Yamada and Ji, 2023), and $0.5 \le A_{\lambda C} \le 3$ satisfied this requirement for all n. In addition, when $A_{\lambda C} = 3$, the natural frequencies of the highest nth-order eigenmodes for $n = 22$, 32, 52, and 92, were 2 kHz, 4 kHz, 8 kHz, and 16 kHz, respectively.

From the simulation results presented in Fig. 2, if $A_{\lambda C}$ is used for the criterion, the tendency of the precision of the natural frequencies does not depend on n. As $A_{\lambda C}$ increased, the precision of the natural frequencies increased. However, when $A_{\lambda C} > 2.7$ was used, the precision decreased. As the lines were not smooth when $A_{\lambda C}$ was relatively large, the condition number of the matrix in the eigenvalue analysis deteriorated. The decrease in precision because of the matrix condition number depends on the software and functions used for the eigenvalue analysis. In the simulations of this study, the eigs function of MATLAB was used, and the inverse of the mass matrix was multiplied by the left side of the stiffness matrix to perform an eigenvalue analysis as a standard eigenvalue problem. Although the tendencies are slightly different between Figs. 2(a) and (b), the range of high precision is almost the same in both cases. Because the horizontal axes were $A_{\lambda C}$ in Fig. 2, the precision is almost independent of n. If l_C is used on the horizontal axes rather than $A_{\lambda C}$, the larger n is more precise than the smaller n.

The simulation results of the RMS of the error rates of the natural frequencies obtained using $A_{\lambda E} = 0$, 1, 1.25, 1.5, 1.75, and 2 are shown in Fig. 3. The material properties listed in Table 1 were used in the simulations. The length l_E was determined such that $A_{\lambda E} = 0$, 1, 1.25, 1.5, 1.75, and 2 when $A_{\lambda C} = 3$ in each case. In all the cases, n was determined such that the natural frequency of the highest nth-order eigenmodes was 16 kHz when $A_{\lambda C} = 3$. Therefore, $n = 86$, 90, 91, 92, 93, and 94 were used for $A_{\lambda E} = 0$, 1, 1.25, 1.5, 1.75, and 2, respectively. The 1st–64th-order eigenmodes were used to calculate the RMS of the error rates of the natural frequencies. $2.5 \le A_{\lambda C} \le 3.5$ performed the best in all cases, independent of $A_{\lambda E}$. As $A_{\lambda E}$ increases, the problem of matrix condition number is more likely to occur.
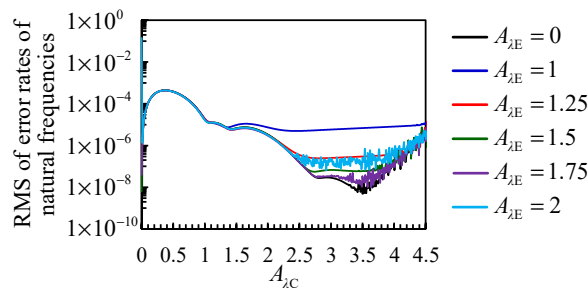

Fig. 3   Simulation results of the RMS of the error rates of the multiple natural frequencies obtained using the SEBM with the SEM and different values of $A_{\lambda E}$.

Although the simulation results were omitted, even if l_A varies while maintaining $l_A + l_B = 0.85\,[\text{m}]$, the tendency that $2.5 \le A_{\lambda C} \le 3.5$ was the best was the same.

The natural frequency of the highest nth-order eigenmode of the original acoustic field was reduced by providing elimination regions. This is the disadvantage of using both SEBM and SEM. Because the appropriate $A_{\lambda C}$ and $A_{\lambda E}$ are $2.5 \le A_{\lambda C} \le 3.5$ and $1.5 \le A_{\lambda E} \le 2$, respectively, when the DOFs of the vibration systems are increased, the ratio of the elimination regions to the length of the original acoustic field is reduced. Therefore, the disadvantage of providing elimination regions is minimal for high-load simulations with many DOFs. $A_{\lambda C}$ and $A_{\lambda E}$ can be determined by referring to Figs. 2 and 3. This study used $A_{\lambda C} = 2.5$ and $A_{\lambda E} = 1.5$ in subsequent simulations because smaller $A_{\lambda C}$ and $A_{\lambda E}$ are advantageous in terms of a wider frequency range.

3.2 Verification on density and bulk modulus of the central virtual elimination region

In the simulations described in Section 3.1, both the density and the bulk modulus of the central elimination region were zero. In this section, the simulation results are presented for small values of density and bulk modulus of the central elimination region. The condition number of a matrix was improved because of the small values. The central elimination region functions as a continuous body. This can reduce the precision of the natural frequencies.

The material properties used in these simulations to verify the density and bulk modulus of the central elimination region were identical to those used in the simulations described in Section 3.1 for the case of $n = 92$, except for the density and bulk modulus of the central elimination region. The simulation results for the error rate magnitude of the first-order natural frequency are shown in Fig. 4. When the central elimination region had density and bulk modulus, new natural frequencies were generated due to them. Therefore, only the first-order natural frequency was used here. The density ratio A_ρ and bulk modulus ratio A_κ are defined as follows:

$$A_\rho = \frac{\rho_C}{\rho_A} = \frac{\rho_C}{\rho_B}, \quad A_\kappa = \frac{\kappa_C}{\kappa_A} = \frac{\kappa_C}{\kappa_B}. \tag{24}$$

$A_\rho = A_\kappa$ was used in these simulations. Under the condition that $A_\rho = A_\kappa$, the sound speeds in regions A and B and the central elimination region are equal, and the precision of the natural frequencies is higher than that when the sound speeds are different. However, the small values of density and bulk modulus in the central elimination regions reduced the precision of the natural frequencies, as shown in Fig. 4. When $A_\rho = A_\kappa = 1 \times 10^{-6}$ was used, the precision was high around $A_{\lambda C} = 1$. In this case, when $A_{\lambda C} < 1$, the natural frequencies obtained by the eigenvalue analysis were slightly higher than the exact natural frequencies, and when $A_{\lambda C} > 1$, they were slightly lower than the exact frequencies. Therefore, they were almost equal to the exact ones around $A_{\lambda C} = 1$. When $A_\rho = A_\kappa = 1 \times 10^{-4}$, 1×10^{-2}, and 1 were used, the natural frequencies obtained by the eigenvalue analysis were slightly lower than the exact frequencies because the mass of the central elimination region affected the natural frequency. As can be seen from Fig. 4, the density and bulk modulus of the central elimination region need not have small values, at least in our simulation environment. When the condition number problem is more likely to occur compared with the authors' simulation environment, A_ρ and A_κ should have sufficiently small values to improve the condition number. In this case, the simulation results shown in Fig. 4 can be used as a reference.
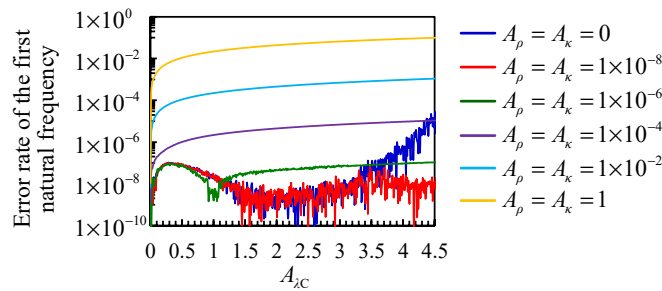

Fig. 4　Simulation results of the magnitude of the error rate of the first-order natural frequency obtained using the SEBM with the SEM and different values of $A_\rho = A_\kappa$.

3.3 Verification to determine the highest order of the eigenmode of the original acoustic field

First, the case in which the sound speeds in regions A and B are equal is described in this section, followed by the case in which they differ. From a series perspective, waves with wavelengths shorter than the wavelength of the highest nth-order eigenmode of the original acoustic field cannot be represented by the superposition of eigenmodes. When the sound speed is a complex number, its imaginary part represents the damping characteristics, and its real part determines the wavelength. Therefore, in this case, the real part of the sound speed should be used to consider the upper limit of the frequency range. Because the imaginary part of the sound speed is not important when considering the upper limit of the frequency range, this section considers a case in which the sound speed is real.

The frequency range in which the natural frequencies can be precisely obtained depends on the natural frequency of the highest nth-order eigenmode of the original acoustic field. Simulations were performed to investigate these frequency ranges. The material properties used in the simulations are listed in Table 2. The sound speeds in regions A and B were equal, and these material properties were also used in the simulations, the results of which are presented in Section 3.4. The cross-sectional area S affects only the results of the simulations performed for verification in Section 3.4, in which a 1-DOF vibration system was installed. As can be seen from Table 2, the actual acoustic field was essentially a 0.85 m acoustic tube, as in the previous simulations, and the exact natural frequencies were integer multiples of 200 Hz. The natural frequencies of the original acoustic fields are integer multiples of $1200/17 \approx 70.6\ [\text{Hz}]$. Therefore, the natural frequency of the highest 17th-order eigenmode of the original acoustic field was 1200 Hz in these simulations. The 1st- to 10th-order natural frequencies obtained using MATLAB's eigenvalue analysis are listed in Table 3. The natural frequencies are listed in ten digits in Table 3, and the error rates in percentages are listed in three digits in Table 3. The precision of the natural frequencies varied significantly at 1200 Hz, which is equal to the natural frequency of the highest nth-order eigenmode of the original acoustic field. Therefore, the frequency range in which the natural frequencies can be precisely obtained is less than that of the highest nth-order eigenmode of the original acoustic field. The precision of the natural frequency at exactly 1200 Hz is slightly lower than that at natural frequencies below 1200 Hz. When the frequency range is limited to a higher precision, the upper limit of the frequency range should be lower than the natural frequency of the highest nth-order eigenmode of the original acoustic field.

In a simulation using SEBM with SEM, l_C, l_E, and n should be determined. Because the natural frequency of the highest nth-order eigenmode depends on l_C, l_E, and n, the natural frequency of the highest nth-order eigenmode is tentatively defined as f_{nT}. f_{nT}, l_C, and l_E can be expressed as

$$f_{nT} = \frac{n c_A}{2l},\ l_C = A_{\lambda CT}\lambda_n,\ l_E = A_{\lambda ET}\lambda_n, \tag{25}$$

Table 2   Material properties used in the simulations for the verification to determine the highest order of the eigenmode of the original acoustic field.

$\rho_A = \rho_B$	1.2 kg/m^3	$\rho_C = \rho_E$	0 kg/m^3	m_C	0 kg
$\kappa_A = \kappa_B$	138720 Pa	$\kappa_C = \kappa_E$	0 Pa	d_C	0 Ns/m
l_A	0.5 m	l_E	$(l_A + l_B)/2$ m	k_C	0 N/m
l_B	0.35 m	$A_{\lambda C}$	2.5	n	17
l_C	$5(l_A + l_B)/6$ m	$A_{\lambda E}$	1.5	S	15000 mm^2

Table 3   Natural frequencies obtained by MATLAB's eigenvalue analysis and their error rates. The natural frequency of the highest nth-order eigenmode of the original acoustic field was 1200 Hz in these simulations.

Exact natural frequencies [Hz]	Calculated natural frequencies [Hz]	Error rate [%]	Exact natural frequencies [Hz]	Calculated natural frequencies [Hz]	Error rate [%]
200	200.0000156	7.78×10^{-6}	1200	1200.029097	2.42×10^{-3}
400	399.9999952	-1.19×10^{-6}	1400	1400.694712	4.96×10^{-2}
600	600.0000332	5.53×10^{-6}	1600	1604.246974	2.65×10^{-1}
800	800.0000106	1.32×10^{-6}	1800	1810.431581	5.80×10^{-1}
1000	1000.000002	2.35×10^{-7}	2000	2125.900877	6.30

respectively, where $A_{\lambda CT}$ and $A_{\lambda ET}$ are the tentative numbers of wavelengths of the central elimination region and elimination regions for the SEM, respectively. Because l_A, l_B, and c_A are given and $A_{\lambda CT}$, $A_{\lambda ET}$, and f_{nT} are arbitrarily determined by the user, from Eqs. (22) and (25), l_C and l_E can be derived as

$$l_C = A_{\lambda CT} \frac{c_A}{f_{nT}}, \quad l_E = A_{\lambda ET} \frac{c_A}{f_{nT}}. \tag{26}$$

From Eqs. (25) and (26), n can be determined as follows:

$$n = \left\lceil \frac{2 f_{nT}(l_A + l_B)}{c_A} + 2 A_{\lambda CT} + 4 A_{\lambda ET} \right\rceil, \tag{27}$$

where the ceiling function was used to make n an integer. Because l_C and l_E are determined using Eq. (26), the true natural frequency of the highest nth-order eigenmode and true number of wavelengths are given by the following equations:

$$f_n = f_{nT} \frac{\left\lceil 2 f_{nT}(l_A + l_B)/c_A + 2 A_{\lambda CT} + 4 A_{\lambda ET} \right\rceil}{2 f_{nT}(l_A + l_B)/c_A + 2 A_{\lambda CT} + 4 A_{\lambda ET}}, \tag{28}$$

$$A_{\lambda C} = A_{\lambda CT} \frac{\left\lceil 2 f_{nT}(l_A + l_B)/c_A + 2 A_{\lambda CT} + 4 A_{\lambda ET} \right\rceil}{2 f_{nT}(l_A + l_B)/c_A + 2 A_{\lambda CT} + 4 A_{\lambda ET}}, \quad A_{\lambda E} = A_{\lambda ET} \frac{\left\lceil 2 f_{nT}(l_A + l_B)/c_A + 2 A_{\lambda CT} + 4 A_{\lambda ET} \right\rceil}{2 f_{nT}(l_A + l_B)/c_A + 2 A_{\lambda CT} + 4 A_{\lambda ET}}. \tag{29}$$

Owing to the rounding off of n in Eq. (27), f_n, $A_{\lambda C}$, and $A_{\lambda E}$ are marginally higher than f_{nT}, $A_{\lambda CT}$, and $A_{\lambda ET}$, respectively. When f_{nT}, $A_{\lambda CT}$, and $A_{\lambda ET}$ are selected such that the ceiling function in Eq. (27) is an integer, the difference does not occur.

When the density and bulk modulus of region B differ from those of region A, the frequency determined by λ_n and the sound speed in region B is important. This frequency is defined as follows:

$$f_{nB} = \frac{c_B}{\lambda_n}, \quad c_B = \sqrt{\frac{\kappa_B}{\rho_B}}, \tag{30}$$

where c_B is the sound speed in region B. At frequencies higher than f_{nB}, the precision cannot be maintained because the wavelength in region B is shorter than λ_n. The smaller one of f_n and f_{nB} is the upper limit of the frequency range. The 1st to 8th natural frequencies for the case where the density and bulk modulus of region B were changed to $5\rho_A$ and $\kappa_A/5$, respectively, and for the case where the density and bulk modulus of region B were changed to $\rho_A/5$ and $5\kappa_A$, respectively, are listed in Table 4. The natural frequencies and error rates are presented as ten and three digits, respectively. Because the characteristic impedance of region B is equal to that of region A in both cases, the exact natural frequencies can be obtained. The impedances of the former and latter region B are equivalent to those of an acoustic field of length $5l_B$ and $l_B/5$, with air density ρ_A and bulk modulus κ_A, respectively. In the former and latter cases, the sound speed is 68 m/s and 1700 m/s, respectively, and f_{nB} is 240 Hz and 6000 Hz, respectively. Therefore, the upper limit of the frequency range is 240 Hz in the former case, and 1200 Hz in the latter case. The precision of the natural frequencies listed in Table 4 is drastically changed before and after these frequencies. Therefore, considering the upper limit of the frequency range based on f_n and f_{nB} is appropriate. When the upper limit of the frequency range is determined by f_{nB}, f_{nT} in Eq. (25) should be multiplied by c_A/c_B.

Table 4　Natural frequencies obtained by MATLAB's eigenvalue analysis and their error rates using $\rho_B = 5\rho_A$ and $\kappa_B = \kappa_A/5$, and $\rho_B = \rho_A/5$ and $\kappa_B = 5\kappa_A$. The upper limits of the frequency range for these cases were 240 and 1200 Hz, respectively.

Case where $\rho_B = 5\rho_A$ and $\kappa_B = \kappa_A/5$ were used			Case where $\rho_B = \rho_A/5$ and $\kappa_B = 5\kappa_A$ were used		
Exact natural frequencies [Hz]	Calculated natural frequencies [Hz]	Error rate [%]	Exact natural frequencies [Hz]	Calculated natural frequencies [Hz]	Error rate [%]
75.55555556	75.55554897	-8.71×10^{-6}	298.2456140	298.2456499	1.20×10^{-5}
151.1111111	151.1111103	-5.26×10^{-7}	596.4912281	596.4912286	8.50×10^{-8}
226.6666667	226.6701244	1.53×10^{-3}	894.7368421	894.7369597	1.31×10^{-5}
302.2222222	302.4003405	5.89×10^{-2}	1192.982456	1192.997440	1.26×10^{-3}
377.7777778	381.5600406	1.00	1491.228070	1495.062880	2.57×10^{-1}
453.3333333	477.8425389	5.41	1789.473684	1805.005533	8.68×10^{-1}
528.8888889	603.2759744	14.1	2087.719298	2380.579642	14.0
604.4444444	725.5655246	20.0	2385.964912	2821.423227	18.3

3.4 Comparison with conventional methods using frequency response function

In this section, the simulation results of the frequency response function obtained using SEBM with SEM and CMSM are compared. In addition, the simulation results obtained using SEBM without SEM and SEM without SEBM are presented and compared with the simulation results obtained using SEBM with SEM. In Fig. 1(b), the case in which all three elimination regions are used is SEBM with SEM, the case in which only the central elimination region is used is SEBM without SEM, and the case in which only the right and left elimination regions are used is SEM without SEBM. Simulations were conducted for cases where the material properties of regions A and B were identical and a 1-DOF vibration system was installed at the interface between regions A and B, and for cases where no 1-DOF vibration system was installed at the interface and the material properties of regions A and B were different. The accuracies of these methods were evaluated based on exact solutions derived using boundary conditions. Therefore, the derivations of the exact solutions and equations of motion based on the CMSM are also briefly described using the analytical model presented in Fig. 1(a).

3.4.1 Derivation of the exact solution using boundary conditions

The wave equations for regions A and B in the analytical models shown in Fig. 1(a) are expressed as

$$\rho_A \frac{\partial^2 \psi_A}{\partial t^2} = \kappa_A \frac{\partial^2 \psi_A}{\partial x_A^2}, \quad \rho_B \frac{\partial^2 \psi_B}{\partial t^2} = \kappa_B \frac{\partial^2 \psi_B}{\partial x_B^2}, \tag{31}$$

respectively, where ψ_A and ψ_B are the displacement potentials of regions A and B, respectively. The equation of motion for the 1-DOF vibration system is derived as

$$m_C \ddot{w}_C + d_C \dot{w}_C + k_C w_C = S\rho_A \left. \frac{\partial^2 \psi_A}{\partial t^2} \right|_{x_A = l_A} - S\rho_B \left. \frac{\partial^2 \psi_B}{\partial t^2} \right|_{x_B = 0}. \tag{32}$$

From Eq. (31), the displacement potentials are derived as

$$\psi_A(x_A, t) = \Psi_A(x_A) e^{j\omega t}, \quad \Psi_A(x_A) = C_{1A} \cos k_A x_A + C_{2A} \sin k_A x_A, \quad k_A = \frac{\omega}{c_A}, \tag{33}$$

$$\psi_B(x_B, t) = \Psi_B(x_B) e^{j\omega t}, \quad \Psi_B(x_B) = C_{1B} \cos k_B x_B + C_{2B} \sin k_B x_B, \quad k_B = \frac{\omega}{c_B}, \tag{34}$$

where ω is the excitation angular frequency, k_A and k_B are the wavenumbers in regions A and B, respectively, and C_{1A}, C_{2A}, C_{1B}, and C_{2B} are constants determined by the boundary conditions. The boundary conditions at the left

and right ends of region A are the displacements $w_L = W_L e^{j\omega t}$ and $w_C = W_C e^{j\omega t}$, respectively. Here, W_L is the amplitude of w_L, and W_C is the complex amplitude of w_C. The boundary condition at the left end of region B is the displacement $w_C = W_C e^{j\omega t}$, and the boundary condition at the right end of region B is zero displacement. Using these four boundary conditions and Eq. (32), C_{1A}, C_{2A}, C_{1B}, C_{2B}, and w_C can be determined.

The sound pressure is obtained using the left-hand sides of Eq. (31). The particle displacements in regions A and B are expressed as $-\partial\psi_A/\partial x_A$ and $-\partial\psi_B/\partial x_B$, respectively.

3.4.2 Conventional modal analysis using the component mode synthesis method

When the CMSM is used (Yamada and Utsuno, 2015), the wave equations for regions A and B in the analytical models shown in Fig. 1(a) are expressed as

$$\rho_A \frac{\partial^2 \psi_A}{\partial t^2} = \kappa_A \frac{\partial^2 \psi_A}{\partial x_A^2} + \kappa_A w_L \delta(x_A) - \kappa_A w_C \delta(x_A - l_A), \quad \rho_B \frac{\partial^2 \psi_B}{\partial t^2} = \kappa_B \frac{\partial^2 \psi_B}{\partial x_B^2} + \kappa_B w_C \delta(x_B). \tag{35}$$

These wave equations include terms for the sound pressure generated by the displacements at the boundaries. The equation of motion for a 1-DOF vibration system is expressed by Eq. (32). In the conventional modal analysis using the CMSM, the displacement potentials ψ_A and ψ_B are given as

$$\psi_A(x_A, t) = \sum_{h=0}^{n_A} \Psi_{Ah}(x_A)\xi_{Ah}(t), \quad \Psi_{Ah}(x_A) = A_{Ah}\cos k_{Ah}x_A, \quad k_{Ah} = \frac{h\pi}{l_A}, \tag{36}$$

$$\psi_B(x_B, t) = \sum_{h=0}^{n_B} \Psi_{Bh}(x_B)\xi_{Bh}(t), \quad \Psi_{Bh}(x_B) = A_{Bh}\cos k_{Bh}x_B, \quad k_{Bh} = \frac{h\pi}{l_B}, \tag{37}$$

respectively, where Ψ_{Ah} and Ψ_{Bh} are the eigenfunctions of the displacement potentials in regions A and B, respectively; n_A and n_B are the highest orders of the eigenmodes for regions A and B, respectively; k_{Ah} and k_{Bh} are the wavenumbers in regions A and B, respectively; and A_{Ah} and A_{Bh} are arbitrary constants. Substituting Eqs. (36) and (37) into Eq. (35), multiplying both sides by Ψ_{Ai}/ρ_A and Ψ_{Bi}/ρ_B, respectively, and integrating over the entire range of regions A and B, the following equations of motion using modal displacements are obtained:

$$M_{Ai}\ddot{\xi}_{Ai} + K_{Ai}\xi_{Ai} = c_A^2 \Psi_{Ai}(0)w_L - c_A^2 \Psi_{Ai}(l_A)w_C, \quad M_{Bi}\ddot{\xi}_{Bi} + K_{Bi}\xi_{Bi} = c_B^2 \Psi_{Bi}(0)w_C, \tag{38}$$

$$M_{Ai} = \int_0^{l_A} (\Psi_{Ai})^2 \, dx_A = 1, \quad K_{Ai} = -c_A^2 \int_0^{l_A} \Psi_{Ai}\frac{d^2\Psi_{Ai}}{dx_A^2}dx_A = \omega_{Ai}^2, \quad \omega_{Ai} = \frac{i\pi c_A}{l_A}, \quad A_{Ai} = \begin{cases} \sqrt{1/l_A} & (i=0) \\ \sqrt{2/l_A} & (i=1,2,\cdots) \end{cases}, \tag{39}$$

$$M_{Bi} = \int_0^{l_B} (\Psi_{Bi})^2 \, dx_B = 1, \quad K_{Bi} = -c_B^2 \int_0^{l_A} \Psi_{Bi}\frac{d^2\Psi_{Bi}}{dx_B^2}dx_B = \omega_{Bi}^2, \quad \omega_{Bi} = \frac{i\pi c_B}{l_B}, \quad A_{Bi} = \begin{cases} \sqrt{1/l_B} & (i=0) \\ \sqrt{2/l_B} & (i=1,2,\cdots) \end{cases}, \tag{40}$$

where M_{Ai}, K_{Ai}, and ω_{Ai} are the modal mass, modal stiffness, and natural angular frequency of the ith-order eigenmode for region A, respectively; and M_{Bi}, K_{Bi}, and ω_{Bi} are the modal mass, modal stiffness, and natural angular frequency of the ith-order eigenmode for region B, respectively. The arbitrary constants A_{Ai} and A_{Bi} were normalized such that $M_{Ai} = 1$ and $M_{Bi} = 1$, respectively. The equation of motion of the 1-DOF vibration system is expressed as

$$m_C\ddot{w}_C + d_C\dot{w}_C + k_C w_C = S\rho_A \sum_{h=0}^{n_A} \Psi_{Ah}(l_A)\ddot{\xi}_{Ah} - S\rho_B \sum_{h=0}^{n_B} \Psi_{Bh}(0)\ddot{\xi}_{Bh}. \tag{41}$$

The equations of motion using matrices can be obtained using Eqs. (36)–(38), and (41). The subsequent modal analysis is identical to that described in Section 2.3.

The sound pressure is obtained using the left-hand sides of Eq. (35). The particle displacements in regions A and B are expressed as $-\partial\psi_A/\partial x_A$ and $-\partial\psi_B/\partial x_B$, respectively. If $-\partial\psi_A/\partial x_A$ and $-\partial\psi_B/\partial x_B$ are derived by integrating

the wave equations over the ranges $0 \le x_A \le x_A$ and $0 \le x_B \le x_B$, respectively, as shown in Eqs. (13) and (14); particle displacements without the Gibbs phenomenon can be obtained. However, this method was not used in the subsequent simulations. This demonstrates the cause of the error in the sound pressure. The Gibbs phenomenon in particle displacement causes errors in the sound pressure.

3.4.3 Simulation results for the cases where a 1-DOF vibration system is installed

The material properties of the acoustic field used in the subsequent simulations were identical to those listed in Table 2. $n = 17$ was used for simulations using SEBM with SEM, SEBM without SEM, and SEM without SEBM. Therefore, the natural frequencies of the highest nth-order eigenmodes for SEBM with SEM, SEBM without SEM, and SEM without SEBM were 1200 Hz, 2400 Hz, and 2200 Hz, respectively. $n_A = 10$ and $n_B = 7$ were used for the simulations using the CMSM, because the DOFs of the acoustic field were equal to those of the other methods if the zeroth-order eigenmodes were omitted. Because the 1-DOF vibration system has one independent DOF in the CMSM, the CMSM used two more DOFs than the other methods when the zeroth-order eigenmodes were included in the count. The natural frequencies of the highest n_A th- and n_B th-order eigenmodes in the CMSM were both 3400 Hz. The material properties of the 1-DOF vibration system used in the subsequent simulations are listed in Table 5, where ζ_C is the damping ratio, defined as $d_C / \left(2\sqrt{m_C k_C} \right)$. The mechanical impedance of the 1-DOF vibration system in Case (1) was 100 times larger than that in Case (2). Therefore, the 1-DOF vibration system in Case (1) had a smaller displacement than that in Case (2).

The simulation results of the nondimensional sound pressure and particle displacement using the material properties of Cases (1) are shown in Fig. 5. Here, P is the complex amplitude of the sound pressure p, W is the complex amplitude of the particle displacement w, and $x = x_3 + 0.05l_B$ was used as the evaluation point. The coordinates in the acoustic field are expressed using x rather than x_A and x_B throughout Section 3.4. The simulation results using the SEBM without the SEM and the SEM without the SEBM did not agree with the exact solutions. However, the simulation result using the SEBM with the SEM agrees well with the exact solutions below 1200 Hz. By using both the SEBM and SEM, high precision can be maintained even for the coordinate near the interface between regions A and B. Because the mechanical impedance of the 1-DOF vibration system is relatively large in Case (1), the simulation results of the nondimensional sound pressure using the CMSM agree well with the exact solutions. However, a slight difference from the exact solution can be seen in the small amplitude region in the sound pressure. The simulation result of the nondimensional particle displacement using the CMSM does not agree well with the exact solution because of the Gibbs phenomenon. When the mechanical impedance of the 1-DOF vibration system is large, the CMSM is advantageous in principle. This is because the eigenmodes that do not have displacement at the coordinate of the 1-DOF vibration system are used in the CMSM. However, even in Case (1), the SEBM with the SEM is better than the CMSM.

The simulation results of the nondimensional sound pressure and particle displacement using the material properties

Table 5 Material properties of the 1-DOF vibration systems used in the simulations.

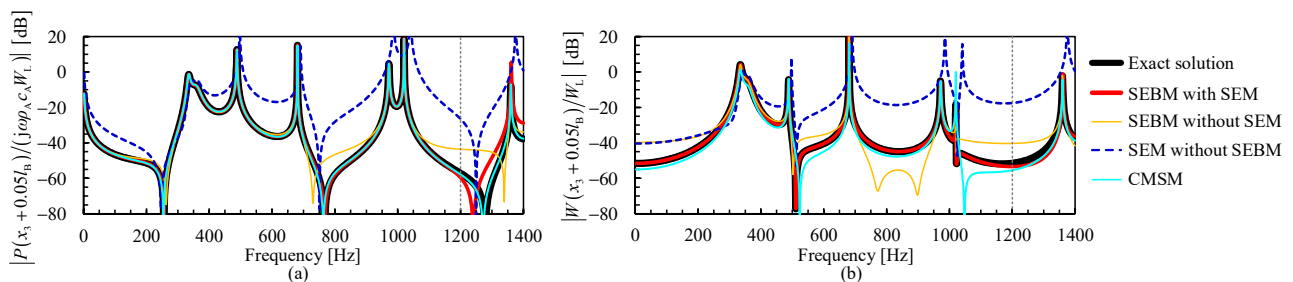|	Case (1)	Case (2)
m_C [kg]	0.3	0.003
k_C [N/m]	1.5×10^6	1.5×10^4
ζ_C	0.05	0.05

Fig. 5 Simulation results of the nondimensional sound pressure and particle displacement when the material properties of Cases (1), listed in Table 5, were used for the 1-DOF vibration system: (a) nondimensional sound pressure and (b) nondimensional particle displacement.

of Case (2) are shown in Fig. 6. The simulation results obtained using SEM without SEBM differed from the exact solutions at approximately 1100 Hz. The simulation results obtained using the SEBM with and without SEM agreed well with the exact solutions. Although the natural frequency of the highest nth-order eigenmode for SEBM with SEM was 1200 Hz, no difference was observed between 1200 Hz and 1400 Hz. This is because methods that use only the eigenmodes of the entire acoustic field are advantageous in principle when the mechanical impedance of the 1-DOF vibration system is small. Because the eigenmodes have a displacement at the coordinate of the 1-DOF vibration system, the displacement at the 1-DOF vibration system can be easily expressed. However, the CMSM is disadvantageous in this case, because the eigenmodes do not exhibit displacement at the coordinate of the 1-DOF vibration system. Therefore, even the resonance peak frequencies differed from those of the exact solutions, as shown in Fig. 6. SEBM combined with SEM provides precise simulation results when the mechanical impedance of the 1-DOF vibration system is both large and small.

The simulation results of the distribution of the nondimensional sound pressure and particle displacement in the acoustic field using the material properties of Case (2) are shown in Fig. 7. Here, the x'-coordinate presented in Fig. 1(a) was used for the horizontal axis, the excitation frequency was 700 Hz, and only steady-state vibrations were considered. These simulation results are the vibration distributions in the acoustic field at the instant of phase when $w_L = W_L$. The simulation results obtained using the SEBM and SEM agree well with the exact solutions. However, the simulation result of the sound pressure using SEBM without SEM differs from the exact solution near the left end. This difference was caused by the Gibbs phenomenon of particle displacement near the left end. Because the Gibbs phenomenon occurred at the left end and at the interface between regions A and B when the CMSM was used, the CMSM simulation results did not agree with the exact solutions. The simulation results of SEM without SEBM did not agree with the exact solutions because the Gibbs phenomenon occurred at the interface between regions A and B.

The simulation results of the vibration distribution, including the elimination regions, are shown in Fig. 8. Here, the x-coordinate was used for the horizontal axis. The installation of the elimination regions smoothly connected the particle displacement and did not cause the Gibbs phenomenon in SEBM with SEM, as intended.

$n = 17$ was used in these simulations. Such a small value of n is relatively disadvantageous for SEBM with SEM because the ratio of the elimination regions is relatively large under this condition, as shown in Fig. 8. However, using a large n increases the number of resonance peaks in the frequency response functions, making it difficult to compare the graphs. Therefore, $n = 17$ was used in the simulations, knowing this disadvantage. As n, n_A, and n_B increase, the
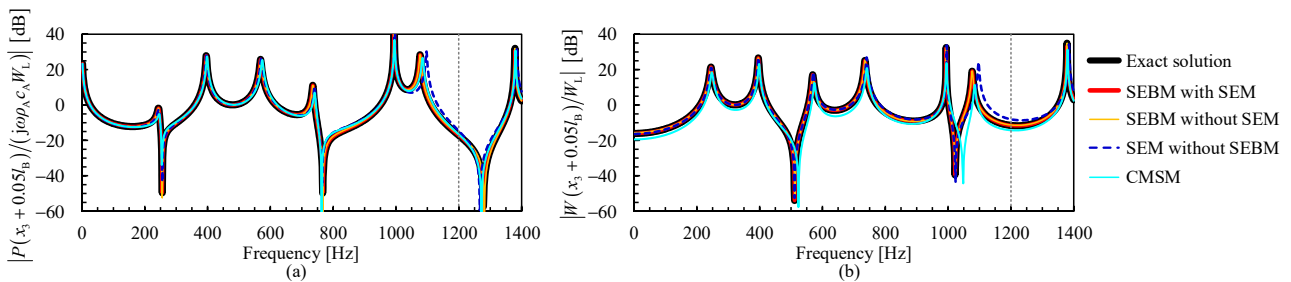

Fig. 6 Simulation results of the nondimensional sound pressure and particle displacement when the material properties of Case (2), listed in Table 5, were used for the 1-DOF vibration system: (a) nondimensional sound pressure and (b) nondimensional particle displacement.
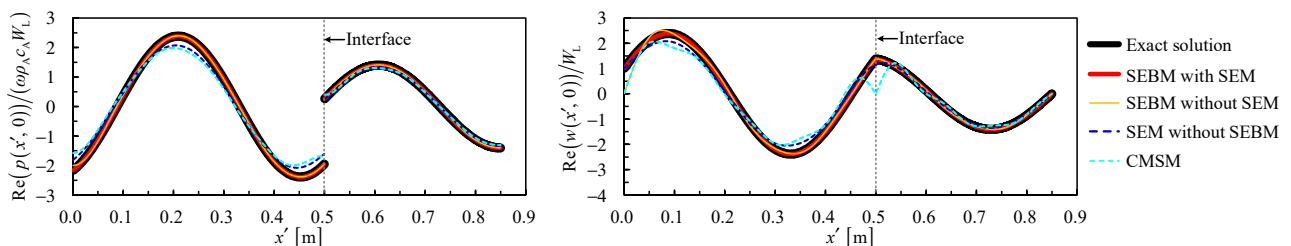

Fig. 7 Simulation results of the distribution of the nondimensional sound pressure and particle displacement in the acoustic field when x'-coordinate and the material properties of Case (2), listed in Table 5, were used. The excitation frequency was 700 Hz. (a) nondimensional sound pressure and (b) nondimensional particle displacement.
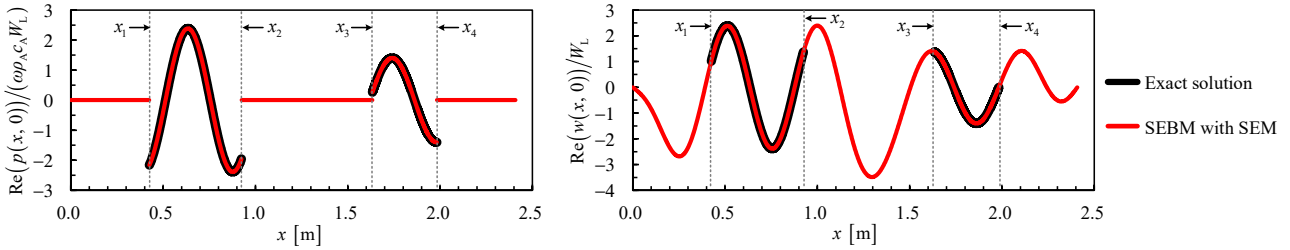
Fig. 8　Simulation results of the distribution of the nondimensional sound pressure and particle displacement in the acoustic field when x-coordinate and the material properties of Case (2), listed in Table 5, were used. The excitation frequency was 700 Hz. The distributions in the elimination regions were also shown. (a) nondimensional sound pressure and (b) nondimensional particle displacement.

precision of the simulations for all methods increases. SEBM with SEM is the most advantageous of these methods when simulations are conducted with fewer DOFs.

In Section 3.3, the way to determine the number of eigenmodes in SEBM with SEM was described. The same approach can be used for CMSM, SEBM without SEM, and SEM without SEBM to determine the number of eigenmodes. However, the Gibbs phenomenon reduces the precision of the simulations in these three methods. Therefore, the number of eigenmodes needs to be further increased in these three methods to reduce the deterioration of the simulation precision.

3.4.4 Simulation results for the cases where the material properties of regions A and B are different

The material properties of region A and the elimination regions used in the subsequent simulations were identical to those listed in Table 2, and a 1-DOF vibration system was not installed. However, $m_C = 1 \times 10^{-8}$ [kg] was used as a sufficiently small value in the CMSM because the 1-DOF vibration system has one independent DOF in this method. The material properties of region B used in the simulations, and n_A and n_B used in the CMSM are listed in Table 6. $n = 17$ was used for simulations using SEBM with SEM, SEBM without SEM, and SEM without SEBM. However, n_A and n_B for the CMSM were determined such that the natural frequencies of the highest n_A th- and n_B th-order eigenmodes were equal and $n_A + n_B$ was approximately 17. Case (a) shows the case in which the acoustic absorption material is installed in region B. The material properties in Cases (b) and (c) do not typically appear in the acoustic field. However, the longitudinal vibration of a rod can have an essentially similar situation. The material properties in Case (b) were used because the sound speed in region B was equal to that in region A. The material properties in Case (c) were used because the sound speed in region B was 1/5 times that of in region A. As discussed in Section 3.3, the upper limits of the frequency range were 712 Hz, 1200 Hz, and 240 Hz in Cases (a)–(c), respectively, when SEBM with SEM was used.

The simulation results of the nondimensional sound pressure and particle displacement using the material properties of Case (a) are shown in Fig. 9. Here, $x = x_1 + 0.95 l_A$ was used as the evaluation point for region A. The particle displacement at the interface between regions A and B was relatively large because a 1-DOF vibration system was not installed in these simulations. Therefore, the simulation results obtained using the CMSM do not agree with the exact solutions. The simulation results of the other three methods agree well with the exact solutions. This is because the evaluation point was $x = x_1 + 0.95 l_A$. Although the simulation results were omitted, SEBM without SEM lost precision near the left end owing to the Gibbs phenomenon. SEM without SEBM and SEBM with SEM maintained their precision in this case. The upper limit of the frequency was 712 Hz in SEBM with SEM. However, precision was maintained even above this frequency, as shown in Fig. 9. This is because the ratio of the length of region B was not large, and the evaluation point was in region A. Although the simulation results were omitted, under the condition that the ratio of the length of region B was large and that the evaluation point was near the right end of region B, the simulation results of SEBM with SEM did not agree with the exact solutions from slightly above 712 Hz.

Table 6　Material properties of region B used in the simulations, and n_A and n_B used in the CMSM.

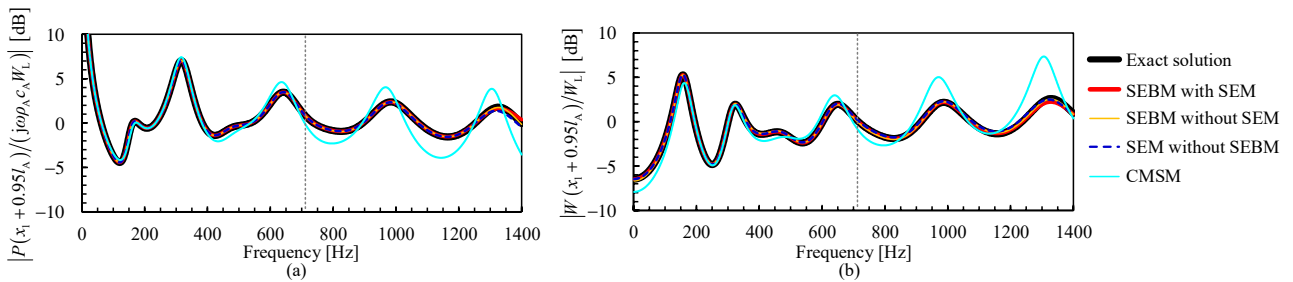|	Case (a)	Case (b)	Case (c)
ρ_B $\lceil \text{kg/m}^3 \rceil$	$2.5(1 - 0.5\text{j})$	$6(= 5\rho_A)$	$6(= 5\rho_A)$
κ_B [Pa]	120000	$693600(= 5\kappa_A)$	$27744(= \kappa_A/5)$
(n_A, n_B)	$(10, 7)$	$(10, 7)$	$(4, 14)$

Fig. 9   Simulation results of the nondimensional sound pressure and particle displacement when the material properties of Cases (a), listed in Table 6, were used for region B. The upper limit of the frequency range was 712 Hz when the SEBM with the SEM was used. (a) nondimensional sound pressure and (b) nondimensional particle displacement.

The simulation results of the nondimensional sound pressure and particle displacement using the material properties of Case (b) are shown in Fig. 10. Here, $x = x_1 + 0.95l_A$ was used. The general tendency was the same as when using the material properties for Case (a). However, in this case, the precision of the SEM without SEBM decreased compared to the simulation using the material properties of Case (a). This is because the characteristic impedance ratio between regions A and B was larger in Case (b) than in Case (a). In this case, only SEBM with SEM maintained precision in all coordinates. In addition, the precision of the SEBM with SEM was maintained below 1200 Hz.

The simulation results of the nondimensional sound pressure and particle displacement using the material properties of Case (c) are shown in Fig. 11. Here, $x = x_1 + 0.95l_A$ was used. Because the upper limit of the frequency was 240 Hz for SEBM with SEM in this case, the frequency response functions below 500 Hz are shown in Fig. 11. The general tendency was the same as when the material properties of Case (b) were used. As the upper limit of the frequency was 240 Hz, the simulation results of SEBM with SEM did not agree well with the exact solutions above 350 Hz. Although omitted here, if the vibration distribution is shown, the difference between SEBM with SEM and the exact solutions can be observed at frequencies above 240 Hz.

SEBM with SEM was better than CMSM when a 1-DOF vibration system was not installed at the interface between regions A and B. Among SEBM with SEM, SEBM without SEM, and SEM without SEBM, SEBM with SEM should be used because SEBM with SEM is no worse than the other two methods, even when $n = 17$.
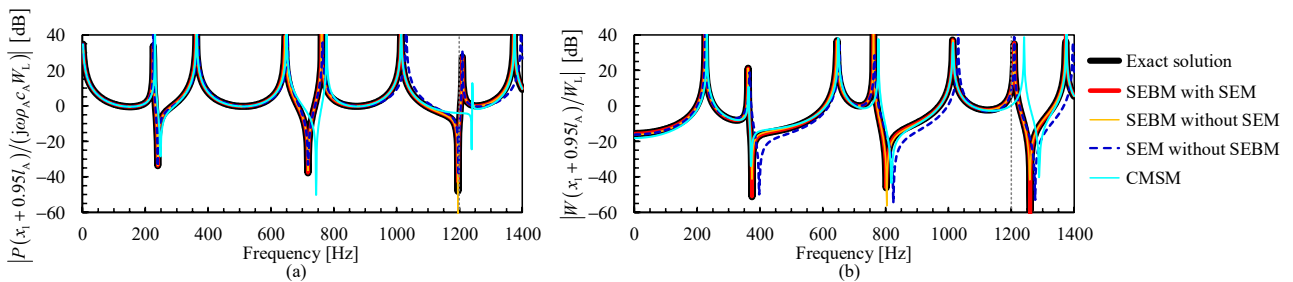

Fig. 10   Simulation results of the nondimensional sound pressure and particle displacement when the material properties of Cases (b), listed in Table 6, were used for region B. The upper limit of the frequency range was 1200 Hz when the SEBM with the SEM was used. (a) nondimensional sound pressure and (b) nondimensional particle displacement.
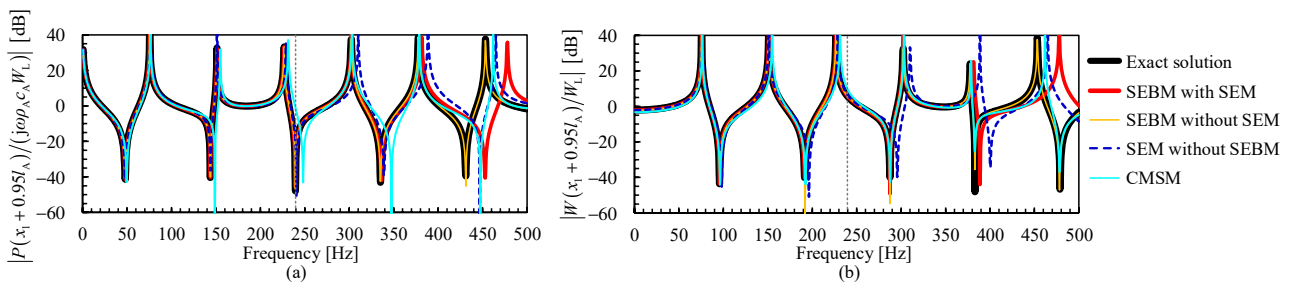

Fig. 11   Simulation results of the nondimensional sound pressure and particle displacement when the material properties of Cases (c), listed in Table 6, were used for region B. The upper limit of the frequency range was 240 Hz when the SEBM with the SEM was used. (a) nondimensional sound pressure and (b) nondimensional particle displacement.

4. Conclusion

SEBM for a continuous body governed by a one-dimensional wave equation was described using a one-dimensional acoustic field as a representative. An analytical model for SEBM with SEM was presented, and the wave equation for this analytical model was derived. Modal analysis was applied to the wave equation, and the external forces applied at the interfaces in the analytical model were formulated using constraint conditions. The simulations revealed that the density and bulk modulus of the virtual elimination region of SEBM should be zero if the deterioration of the matrix condition number is not problematic. The simulations also revealed that the length of the virtual elimination region of the SEBM should be set to 2.5–3.5 times the wavelength of the highest eigenmode when eigenvalue analysis is performed as a standard eigenvalue problem using an inverse matrix of the mass matrix in the simulations using MATLAB. The formulations for determining the order of the highest-order eigenmode and the length of the virtual elimination regions were derived based on the upper limit of the frequency range. The frequency response functions obtained using SEBM with and without SEM, SEM without SEBM, and CMSM were compared based on the exact solutions, and it was found that the precision of the CMSM decreased when the displacement at the interface between the different regions was relatively large, and the precision of SEBM without SEM and SEM without SEBM decreased when the displacement at the interface was relatively small. However, SEBM with SEM maintained precision in all cases. Because the wavelength of the highest-order eigenmode becomes shorter as the number of employed eigenmodes increases, the ratio of the lengths of the elimination regions to the overall lengths becomes smaller. Therefore, SEBM with SEM is more advantageous when the targeted continuous body requires more DOFs.

Acknowledgment

References

Benaroya, H. and Nagurka, M. L., Mechanical Vibration: Analysis, Uncertainties, and Control, Third edition (2009), CRC Press.

Bishop, R. E. D. and Johnson, D. C., The Mechanics of Vibration (1960), Cambridge University Press.

Hale, A. L. and Meirovitch, L., A general substructure synthesis method for the dynamic simulation of complex structures, Journal of Sound and Vibration, Vol. 69, Issue 2(1980), pp. 309–326.

Meirovitch, L., Analytical Methods in Vibrations (1967), Macmillan.

Meirovitch, L., Dynamics and Control of Structures (1990), John Wiley & Sons.

Meirovitch, L., Fundamentals of Vibrations (2001), McGraw-Hill Higher Education.

Nagamatsu, A., Modal Analysis (1985), Baifukan (in Japanese).

Ookuma, M. and Nagamatsu, A., Vibration analysis by substructure synthesis method (Part 4, Calculation of residual compliance matrix), Bulletin of the Japan Society of Mechanical Engineers, Vol. 28, No. 239(1985), pp. 905–910.

Ookuma, M. and Nagamatsu, A., Vibration analysis by component mode synthesis method (Comparison of three methods (I)), Bulletin of the Japan Society of Mechanical Engineers, Vol. 29, No. 249(1986), pp. 882–887.

Rao, S. S., Vibration of Continuous Systems (2007), John Wiley & Sons.

Reismann, H., Elastic Plates: Theory and Application (1988), John Wiley & Sons.

Shabana, A. A., Substructure synthesis methods for dynamic analysis of multi-body systems, Computers & Structures, Vol. 20, No. 4(1985), pp. 737–744.

Shabana, A. A., Theory of Vibration: Volume II: Discrete and Continuous Systems (1991), Springer-Verlag New York, Inc.

Tanaka, N., Takara, Y., and Iwamoto, H., Eigenpairs of a coupled rectangular cavity and its fundamental properties, Journal of the Acoustical Society of America, Vol. 131, No. 3(2012), pp. 1910–1921.

Yamada, K., Proposal of substructure change or elimination method, Dynamics and Design Conference (2017), p. 440(12

pages) (in Japanese).

Yamada, K., Vibration analysis using substructure change and elimination methods, Proceedings of the 25th International Congress on Sound and Vibration (2018), p. 485(8 pages).

Yamada, K., Coupled vibration analysis of acoustic field including flexible structures, Proceedings of the 15th International Conference on Motion and Vibration Control (2020), Paper ID: 10062(10 pages).

Yamada, K. and Ji, J., Substructure elimination method for vibration systems governed by a one-dimensional wave equation, Mechanical Engineering Journal, Vol. 10, No. 5(2023), DOI: 10.1299/mej.23-00241.

Yamada, K. and Ji, J., Substructure elimination method for evaluating bending vibration of beams, Mechanical Engineering Journal, Vol. 10, No. 6(2023), DOI: 10.1299/mej.23-00293.

Yamada, K. and Utsuno, H., Theoretical analysis of vibration of continuous body using replacement of displacement excitation with force excitation, Proceedings of the 22nd International Congress on Sound and Vibration (2015), p. 428(8 pages).

Yamada, K. and Utsuno, H., Modal analysis of continuous systems by replacing displacement excitation with equivalent excitation force and fixed boundary, Mechanical Engineering Journal, Vol. 7, No. 4(2020), DOI: 10.1299/mej.20-00003.